

Concurrence of Quantum Anomalous Hall and Topological Hall Effects in Magnetic Topological Insulator Sandwich Heterostructures

Jue Jiang^{1,4}, Di Xiao^{1,4}, Fei Wang¹, Jae-Ho Shin¹, Domenico Andreoli², Jianxiao Zhang¹, Run
Xiao¹, Yi-Fan Zhao¹, Morteza Kayyalha¹, Ling Zhang¹, Ke Wang³, Jiadong Zang², Chaoxing
Liu¹, Nitin Samarth¹, Moses H. W. Chan¹, and Cui-Zu Chang¹

¹Department of Physics, The Pennsylvania State University, University Park, PA 16802

²Department of Physics, University of New Hampshire, Durham, NH 03824

³Materials Research Institute, The Pennsylvania State University, University Park, PA 16802

⁴These authors contributed equally to this work.

Corresponding authors: nxs16@psu.edu (N.S.); mhc2@psu.edu (M.H.W.C.); cxc955@psu.edu
(C.Z.C.)

The quantum anomalous Hall (QAH) effect is a quintessential consequence of non-zero Berry curvature in momentum-space. The QAH insulator harbors dissipation-free chiral edge states in the absence of an external magnetic field. On the other hand, the topological Hall (TH) effect, a transport hallmark of the chiral spin textures, is a consequence of real-space Berry curvature. While both the QAH and TH effects have been reported separately, their coexistence, a manifestation of entangled chiral edge states and chiral spin textures, has not been reported. Here, by inserting a TI layer between two magnetic TI layers to form a sandwich heterostructure, we realized a concurrence of the TH effect and the QAH effect through electric field gating. The TH effect is probed by bulk carriers, while the QAH effect is characterized by chiral edge states. The appearance of TH effect in the QAH insulating regime is the consequence of chiral magnetic domain walls that result from the gate-induced

Dzyaloshinskii-Moriya interaction and occur during the magnetization reversal process in the magnetic TI sandwich samples. The coexistence of chiral edge states and chiral spin textures potentially provides a unique platform for proof-of-concept dissipationless spin-textured spintronic applications.

Electronic band structures of nontrivial topology in momentum-space and magnetic chiral spin textures in real-space have attracted enormous attention in the past decade since they harbor elegant Berry curvature physics^{1,2,3}. The intrinsic anomalous Hall (AH) effect is such an example: it is induced by the Berry curvature in momentum-space in ferromagnetic (FM) materials⁴ and can even be quantized under certain circumstances, leading to the quantum anomalous Hall (QAH) effect. The QAH effect has been theoretically proposed^{5,6,7,8} and experimentally realized^{9,10,11,12,13} in magnetically doped topological insulator (TI) films. On the other hand, chiral spin textures (e.g. skyrmions) provide another example of nontrivial topology, but in real-space. It has been shown that chiral spin textures can also induce a Hall current: this is known as the topological Hall (TH) effect and is generally regarded as the transport signature of non-zero spin chirality³. The TH effect has been experimentally observed in many *metallic* systems, such as MnSi^{14,15}, MnGe¹⁶, FeGe¹⁷, and SrIrO₃/SrRuO₃ interface^{18,19} as well as magnetically doped TI films and heterostructures^{20,21}. The TH effect in these systems is usually observed accompanied by the AH effect. However, there is no conclusive evidence to date that the AH effect found in these *metallic* systems to be intrinsic, i.e., exclusively induced by the momentum-space Berry curvature⁴.

The QAH and TH effects have been separately observed in magnetically doped TI^{9,10,20,21}, with distinctly different sample geometries. The QAH effect can be realized only in the *insulating* regime of a magnetic TI^{9,10,11,12,13} while the TH effect is usually seen in *metallic* systems^{20,21}. In this *Article*, we realized the TH effect in the *insulating* regime of magnetic TI and demonstrated

the concurrence of the QAH and TH effects in a single sample. This concurrence provides a new platform to understand the interplay between chiral edge states of the QAH effect and chiral spin textures associated with the TH effect.

In order to realize the QAH and TH effects in one TI-based device, the sample needs to accommodate the following three conditions: (i) The time-reversal symmetry is broken, which is the common prerequisite for both QAH and TH effects; (ii) The chemical potentials of the top and bottom surfaces can be simultaneously tuned near the magnetization exchange gaps, which is essential for the QAH effect; (iii) A significant Dzyaloshinskii-Moriya (DM) interaction, $H = \mathbf{D}_{ij} \cdot (\mathbf{S}_i \times \mathbf{S}_j)$, can be created, which is required for the TH effect. Recently, two papers reported the observation of the TH effect in TI. Yasuda *et al*²⁰ fabricated the Cr-(Bi,Sb)₂Te₃/(Bi,Sb)₂Te₃ bilayer structures, where only one surface is gapped owing to the magnetic exchange interaction. The consequential spatial asymmetry thus favors the formation of the DM interaction and gives rise to the TH effect in this bilayer structure when it is tuned into the *p*-type *metallic* regime. However, the QAH effect cannot be realized in such a bilayer sample geometry since the other surface is non-magnetic and gapless. Liu *et al*²¹ grew 4 quintuple layers (QL) Mn-doped Bi₂Te₃ films without a Te capping layer on a SrTiO₃ substrate, revealing the TH effect in both *p*- and *n*-type *metallic* regimes. Since the Dirac point is buried under the bulk valence bands in Bi₂Te₃ films^{22, 23}, the QAH state is also unlikely in Mn-doped Bi₂Te₃ samples. In uniformly doped QAH samples, the inversion symmetry is preserved in the bulk^{9, 10}, so that the DM interaction is induced only on the top and bottom surfaces^{24, 25}. However, the DM interactions from the two opposite surface states (SSs) have opposite signs. When the two surfaces are strongly coupled, spin chirality cannot be achieved. Effectively, the overall DM interaction felt by the magnetization is greatly reduced and it is difficult to realize the TH effect in such uniformly doped QAH samples. Therefore,

to realize the concurrence of the QAH and TH effects in a single sample, the two surfaces of a QAH sample should be separated and inversion symmetry must be broken, in order to induce finite DM interaction.

We fabricated a TI-based sandwich structure with an undoped TI layer (5 QL $(\text{Bi, Sb})_2\text{Te}_3$ layers) inserted between two magnetic TI layers (two 3 QL Cr-doped $(\text{Bi, Sb})_2\text{Te}_3$ layers) (**Figs. 1a** and **1b**). Such a 3-5-3 sandwich heterostructure has two distinct advantages. First, the nonmagnetic TI layer serves as a spacer that separates the magnetic exchange interaction between the two magnetic TI layers^{26, 27, 28}. As a result, the influence of the DM interaction can be maximized since the magnetic moments in each magnetic TI layer interacts only with their own SS. Second, both the top and bottom SSs are separately gapped by the magnetization, thus making the QAH effect possible. The magnetic/nonmagnetic/magnetic TI sandwich heterostructures were grown on 0.5 mm thick $\text{SrTiO}_3(111)$ substrates in a molecular beam epitaxy (MBE) chamber with a base vacuum $\sim 2 \times 10^{-10}$ mbar. The transport studies were carried out in a dilution refrigerator (Leiden Cryogenics, 10 mK, 9 T) and a Physical Property Measurement System (Quantum Design, 2 K, 9 T) with the magnetic field applied perpendicular to the film plane. Six-terminal Hall bars with bottom-gate electrodes (**Fig. 1a**) were used for transport studies.

We now focus on the transport results of the 3-5-3 heterostructure. When the bottom gate $V_g = 0$ V, the FM order at low temperatures gaps out the top and bottom SSs, and the chemical potential is located inside the magnetic exchange gaps of both surfaces (**Fig. 1b**). This is confirmed by the observation of a perfectly quantized Hall resistance (ρ_{yx}) and a vanishing longitudinal resistance (ρ_{xx}) at $T = 30$ mK (**Figs. 1c** and **1d**). With increasing temperature, the sample deviates from the QAH state and shows transport properties of a conventional FM material, namely, hysteretic ρ_{yx}

loops and butterfly-shaped ρ_{xx} . The Curie temperature (T_C) of the 3-5-3 sandwich heterostructure sample is determined to be ~ 19 K by means of Arrott plots (**Fig. S4**).

Figure 2 shows the magnetic field $\mu_0 H$ dependence of the Hall resistance ρ_{yx} and the longitudinal resistance ρ_{xx} of the 3-5-3 heterostructure at different gate voltages ($V_g - V_g^0$). When $V_g = V_g^0 = +20$ V, the sample displays a perfect QAH state: at zero magnetic field, $\rho_{yx}(0) = \pm h/e^2$ and $\rho_{xx}(0) < 1 \Omega$. When the magnetic field $\mu_0 H > \mu_0 H_c$ ($\mu_0 H_c$ is the coercive field), the Hall curves completely overlap during upward and downward magnetic field sweeps (**Fig. 2d**). When $(V_g - V_g^0) = -100$ V, hole carriers are injected into the sample and dissipative bulk channels are introduced. In this regime, $\rho_{yx}(0)$ deviates from h/e^2 but still remains as high as $\sim 0.76 h/e^2$ and $\rho_{yx}(0)/\rho_{xx}(0) \sim 1.2$, indicating the persistence of the chiral edge transport of the QAH state⁹. The existence of chiral edge transport is further supported by the decrease in $\rho_{xx}(0)$ with decreasing temperature (**Fig. 3e**), which we will discuss in detail below. Notably, over a range of a fraction of a Tesla above $\mu_0 H_c$, a “hump” feature appears in the ρ_{yx} curves (green shadow area); specifically, the Hall curve under downward $\mu_0 H$ sweep does not overlap with that under upward $\mu_0 H$ sweep when $\mu_0 H > \mu_0 H_c$ (**Fig. 2c**). The “hump” feature observed here has been interpreted as a signature of the TH effect and is considered as strong evidence for the existence of chiral spin textures in real-space^{3, 14, 15, 16, 17, 18, 19, 20, 21}. Therefore, by adjusting the chemical potential using the bottom gate, we have realized the concurrence of QAH and TH effects in the *insulating* regime of the magnetic TI sandwich sample. This “hump” feature of TH effect becomes more pronounced when the chemical potential is further tuned towards the bulk valence bands (**Figs. 2a and 2b**).

At $(V_g - V_g^0) = +70$ V, electron carriers are introduced, a trace of the “hump” feature of TH effect also appears (**Fig. 2e**). The observation of $\rho_{yx}(0) \sim 0.85 h/e^2$ and $\rho_{yx}(0)/\rho_{xx}(0) \sim 4.6$

demonstrates the existence of the QAH state. Therefore, the QAH effect is also concurrent with the TH effect for $(V_g - V_g^0) = +70\text{V}$. When more electrons are introduced, the ‘‘hump’’ feature of TH effect fades away (**Fig. 2f**). The asymmetric behavior of the TH effect in n - and p -type regions is possibly a result of the non-symmetric electronic band structure of TI^{23,29}, which we will discuss below. We note that the slope of the Hall traces at high magnetic fields ($0.5\text{ T} < \mu_0H < 1.5\text{ T}$) is always negative in both $V_g < V_g^0$ and $V_g > V_g^0$ regions, which suggests that the standard Hall coefficient R_N cannot be used to estimate carrier density near the QAH regime (see **Fig. S9** and relevant discussion).

In a FM material, the total ρ_{yx} is a result of three contributions: the normal Hall (NH) resistance ρ_{yx}^{NH} , the AH resistance ρ_{yx}^{AH} , and the TH resistance ρ_{yx}^{TH} ,

$$\rho_{yx} = \rho_{yx}^{\text{NH}} + \rho_{yx}^{\text{AH}} + \rho_{yx}^{\text{TH}} \quad (1)$$

In order to single out the TH component ρ_{yx}^{TH} , we need to subtract ρ_{yx}^{NH} and ρ_{yx}^{AH} from ρ_{yx} . Here we interpret the offset resistance under upward and downward μ_0H sweeps (green shadow area in **Fig. 2**) as ρ_{yx}^{TH} for the following reasons. Let us consider the positive μ_0H regime: During the downward μ_0H sweep (red curves in **Fig. 2**), the system should be in a FM state without any chiral spin textures and thus ρ_{yx} should include ρ_{yx}^{NH} and ρ_{yx}^{AH} . For the upward μ_0H sweep (blue curves in **Fig. 2**), the system undergoes a magnetic transition around μ_0H_c and chiral spin textures, particularly chiral magnetic domain walls (see relevant discussion on **Figs. 4a** and **4b** below), can be formed. In this situation, all three Hall contributions are present and $\rho_{yx}^{\text{NH}} + \rho_{yx}^{\text{AH}}$ keeps the same value during the downward μ_0H sweep. Thus, ρ_{yx}^{TH} can be extracted by the difference between the red and blue curves²¹. We emphasize that the standard expressions for ρ_{yx}^{NH} and ρ_{yx}^{AH} ($\rho_{yx}^{\text{NH}} = \mu_0 R_N H$ and $\rho_{yx}^{\text{AH}} = R_A M$ with the AH coefficient R_A and the sample magnetization M ^{9,30,31})

are applicable only for *metallic* systems and thus not valid for our samples close to the QAH *insulating* regime (see **Fig. S9** and relevant discussion). When $(V_g - V_g^0) = -220$ V, the maximum of ρ_{yx}^{TH} is ~ 1.65 k Ω , which is much larger than the TH resistances observed in all previous studies on *metallic* systems^{3, 14, 15, 16, 17, 18, 19, 20, 21}.

To locate the region for the coexistence of the QAH and TH effects, we summarize the $(V_g - V_g^0)$ dependence of $\rho_{yx}(0)$, $\rho_{xx}(0)$, and ρ_{yx}^{TH} at $T=30$ mK (**Figs. 3a** and **3b**). When -30 V $\leq (V_g - V_g^0) \leq +40$ V, the sample exhibits a perfect QAH state, i.e. $\rho_{yx}(0)$ is fully quantized, $\rho_{xx}(0)$ and ρ_{yx}^{TH} are vanishingly small. The perfect QAH state is further validated by the temperature dependence of $\rho_{xx}(0)$ and $\rho_{yx}(0)$ (**Fig. 3f**). When $(V_g - V_g^0)$ is tuned from -30 V to -140 V, the sample shows the non-perfect QAH state, where the current flows through both the dissipationless chiral edge channels and the dissipative bulk channels³². $\rho_{yx}(0)$ decreases from $\sim h/e^2$ to $\sim 0.59 h/e^2$, while $\rho_{xx}(0)$ increases from ~ 0 to $\sim 0.87 h/e^2$. As noted above, the existence of the QAH state for $(V_g - V_g^0) = -100$ V and -140 V can be further confirmed by the decrease in $\rho_{xx}(0)$ and the increase in $\rho_{yx}(0)$ with decreasing temperature (**Figs. 3d** and **3e**). The opposite temperature dependences of $\rho_{xx}(0)$ and $\rho_{yx}(0)$, together with the large $\rho_{yx}(0)/\rho_{xx}(0)$ ratio, can only be a result of the chiral edge states, thus providing conclusive evidence for the existence of the QAH state. Simultaneously, ρ_{yx}^{TH} increases monotonically between -140 V and -30 V for $(V_g - V_g^0)$, demonstrating the presence of the TH effect as well as the QAH effect. In other words, the chiral spin textures coexist with chiral edge states. When $(V_g - V_g^0)$ is further tuned from -140 V to -220 V, the signature of the QAH state disappears, with $\rho_{xx}(0)$ and $\rho_{yx}(0)$ showing similar temperature dependence (**Fig. 3c**), only TH effect is seen in this regime.

The QAH state persists for $(V_g - V_g^0)$ greater than $+40$ V up to $+100$ V with $\rho_{yx}(0) \sim 0.49 h/e^2$, and $\rho_{yx}(0)/\rho_{xx}(0) \sim 1.1$. The presence of the QAH state at $(V_g - V_g^0) = +70$ V is also verified by the

decrease in $\rho_{xx}(0)$ and the increase in $\rho_{yx}(0)$ with decreasing temperature (**Fig. 3g**). In this regime, a smaller ρ_{yx}^{TH} as compared to the p -doped regime (i.e. $V_g < V_g^0$) is found. Therefore, for $+40 \text{ V} < (V_g - V_g^0) \leq +100 \text{ V}$, the TH effect is also concurrent with the QAH effect. When $(V_g - V_g^0)$ is further increased from $+100 \text{ V}$ to $+180 \text{ V}$, the similar temperature dependence of $\rho_{xx}(0)$ and $\rho_{yx}(0)$ marks the disappearance of the QAH state (**Fig. 3h**), only TH effect is seen. The much smaller ρ_{yx}^{TH} for $V_g > V_g^0$ indicates that the chemical potential of the system has not crossed the bulk conduction bands. As we discuss in detail below, this implies that the TH feature at $V_g > V_g^0$ is solely induced by the asymmetric potential between the top and bottom surfaces crossing the helical SSs^{32,33}.

Figure 3i shows the $\mu_0 H$ dependence of ρ_{yx}^{TH} with the maximum peak at different temperatures under $V_g = V_g^{\text{TH}, \text{max}}$. ρ_{yx}^{TH} decreases gradually with temperature from 30mK and disappears at $T = 5 \text{ K}$. The peak position of ρ_{yx}^{TH} and the magnetic field range of the “hump” feature also monotonically decreases with increasing T . We summarize the peak value of ρ_{yx}^{TH} (i.e. $\rho_{yx}^{\text{TH}, \text{max}}$) as a function of $(V_g - V_g^0)$ at different temperatures. The ρ_{yx}^{TH} curve at each T is asymmetric between $V_g < V_g^0$ and $V_g > V_g^0$. When $60 \text{ mK} \leq T \leq 1 \text{ K}$, the ρ_{yx}^{TH} shows a peak when $V_g < V_g^0$ (**Fig. S7g**). This observation indicates the DM interaction strength is maximized when the chemical potential crosses the bulk valence bands.

In order to understand the experimental observations, we propose a model based on the emergence of chiral spin textures around the $\mu_0 H_c$ regime. The observed “hump” structure in ρ_{yx} has been observed in a variety of noncollinear magnetic systems, particularly skyrmion systems^{14, 15, 16, 17}, and is regarded as the key signature for the chirality of skyrmions. However, our sample has a robust FM ground state for the occurrence of the QAH effect at low $\mu_0 H$, thus stable skyrmions are unlikely to be formed³⁴. Our theoretical calculation (see **Fig. S17** and relevant discussion) confirms that the magnetic TI sample is dominated by FM states (i.e. Heisenberg

magnetic coupling). Since the TH effect only occurs near the $\mu_0 H_c$ regime, this fact motivates us to consider the possible chiral spin textures during magnetization reversal. During a FM transition, magnetic domains with opposite polarization are nucleated. The presence of strong DM interaction gives rise to chiral walls at domain boundaries (**Figs. 4a** and **4b**). Net scalar chirality $Q = \sum \mathbf{S}_1 \cdot (\mathbf{S}_2 \times \mathbf{S}_3)$ is thus non-zero and leads to the TH effect. This is similar to the emergent chirality reported in Refs. ^{35, 36, 37}, where magnetization reversal is driven by thermal fluctuations. The DM interaction is essential since chirality is caused by the canting of neighboring spins. Furthermore, since the scalar chirality Q respects full rotational symmetry while the DM interaction strength D breaks inversion symmetry, $Q \sim D^2$. The TH effect observed in our experiment can thus be understood qualitatively by investigating the DM interaction in magnetic TI sample.

The DM interaction is attributed to the strong spin-orbit coupling in our system. It can be computed via the spin susceptibility of a simplified model for TI films ³⁸. The Hamiltonian consists of two parts: the SS Hamiltonian H_{SS} and the bulk state Hamiltonian H_{QW} that describes the quantum well (QW) states due to the quantum confinement effect (see **Section VI** in Supplementary Information). The energy dispersions of the SS and QW bands are shown in **Fig. 4c**. For simplicity, only one set of QW bands are included, but the inclusion of more QW bands is straightforward and does not affect the qualitative physical picture. The Dirac cones of SS bands are close to the valence band top, and this is consistent with the early theoretical and experimental studies ^{32, 33, 39}. Electrons couple to the magnetization \mathbf{M} via $H_{Zeeman} = -\mathbf{M} \cdot \mathbf{\Gamma}$, where $\mathbf{\Gamma}$ are proper 4×4 matrices for electron spin operators. The spin susceptibility $\chi_{\alpha\beta}(\alpha, \beta = x, y, z)$ is evaluated for the model Hamiltonian based on linear response theory $\chi_{\alpha\beta}(\mathbf{q}) = \frac{T}{2V} \text{Tr}[G_0(\mathbf{q} + \mathbf{k}, i\omega_m)\Gamma_\alpha G_0(\mathbf{k}, i\omega_m)\Gamma_\beta]$. The DM interaction is given by $D_\alpha(\mathbf{q}) = \varepsilon_{\alpha\beta\gamma}\chi_{\beta\gamma}(\mathbf{q})$ where ε is the Levi-Civita symbol. As the system breaks mirror symmetry with respect to xy -plane, $\chi_{xy} = 0$, we

thus focus on the off-diagonal components χ_{xz} and χ_{yz} . As expected from the Moriya rule⁴⁰, χ_{xz} (χ_{yz}) is linearly proportional to the momentum q_x (q_y) (**Fig. S18**). By choosing a nonzero q_x value, we calculated χ_{xz} as a function of energy for the QW states and SSs with different asymmetric potential U (**Figures 4d** and **4e**) and found a nonzero U is indeed required to break the inversion symmetry and induce finite χ_{xz} . Note that in the real samples, in addition to the chemical potential (μ), U also depends on V_g , but as discussed in Supplementary Information, its dependence on V_g is much weaker in our experiment. The SSs contribution to χ_{xz} shows a double peak structure around the charge neutral point. For the bulk QW states, χ_{xz} reveals a peak when μ lies between two spin-split (valence) bands and then drops and even changes its sign when μ crosses both spin bands. The bulk conduction band is well above the energy range of interest (-30~40 meV) and thus does not contribute. **Figure 4f** shows the total χ_{xz} , which behaves similarly as ρ_{yx}^{TH} in our experiment (**Fig. 3b**). The large asymmetry between the electron and hole doping sides arises because the SS is close to the valence band but well below the conduction band. At $V_g < V_g^0$, a large contribution to χ_{xz} from the bulk valence band top significantly enhances the DM interaction and ρ_{yx}^{TH} in consequence. We note that including more bulk QW states in the model can further enhance the DM interaction in the hole doping regime. On the other hand, the SS contribution prevails in the $V_g > V_g^0$ regime. When μ is high above the charge neutral point, χ_{xz} vanishes, which is consistent with ρ_{yx}^{TH} in the electron doping regime.

We note that χ_{xz} is non-zero near the charge neutral point, but in our experiment ρ_{yx}^{TH} is not seen, particularly at low temperatures. This is because in the perfect QAH regime there are no bulk carriers to probe the chiral spin textures. This scenario is validated through numerical simulation of the TH effect for a single chiral domain wall (see **Section VII** in Supplementary Information). At higher temperatures (0.4 K ~ 3 K), bulk carriers can be thermally excited and ρ_{yx}^{TH} gradually

decreases (**Figs. 3i** and **S7g**). At even higher temperature (> 5 K), the vanishing of ρ_{yx}^{TH} is the result of the fact that the thermal fluctuation is larger than the energy scale of DM interaction and thus destroys the chirality of magnetic domain walls.

A recent experiment has suggested an alternative interpretation of the “hump” feature of ρ_{yx} observed in the SrIrO₃/SrRuO₃/SrTiO₃ sandwich structures⁴¹. Here, the SrIrO₃/SrRuO₃ and SrRuO₃/SrTiO₃ interfaces have opposite signs of the AH contribution and different $\mu_0 H_c$. In their sandwich sample, the antiferromagnetic alignment configuration between the two magnetic interfaces will induce a larger ρ_{yx} than the FM alignment. This can lead to the TH effect-like “hump” structure. However, this scenario is unlikely to occur in our samples for several reasons: First, ρ_{yx} with a negative sign together with a significantly enhanced $\mu_0 H_c$ has *never* been observed in Cr-doped (Bi,Sb)₂Te₃ samples. Second, as a control experiment, we grew 5QL V-doped TI (Bi,Sb)₂Te₃ on top of the 3-5-3 sandwich sample and used the exchange coupling to increase the $\mu_0 H_c$ of the top Cr-doped TI layer. This structure configuration favors the formation of the antiferromagnetic alignment between top and bottom Cr-doped TI layers. The “hump” feature in this control sample, however, disappears rather than being enhanced (**Fig. S16**). Finally, our magnetization measurements show no additional step near $\mu_0 H_c$ in our samples (**Fig. S3**).

To summarize, we fabricated magnetic TI sandwich heterostructures and observed the concurrence of the QAH and TH effects by applying an electrostatic gating voltage. This concurrence indicates an interplay between the chiral edge states and the chiral spin textures in magnetic TI heterostructures that deserves further experimental and theoretical studies. The chiral spin texture associated with the TH effect can be utilized to record the spin information³⁴, and this spin information can be transferred through the chiral edge channels of the QAH effect. The

marriage of chiral edge states and chiral spin textures potentially opens the door for further explorations of proof-of-concept magnetic TI-based spintronic and electronic devices.

Methods

MBE growth of TI sandwich heterostructure.

The magnetic TI sandwich heterostructure growth was carried out using a Veeco/Applied EPI MBE system with a vacuum $\sim 2 \times 10^{-10}$ mbar. The heat-treated insulating SrTiO₃ (111) substrates were outgassed at ~ 530 °C for 1 hour before the growth of the TI sandwich heterostructures. High-purity Bi (5N), Sb (6N), Cr (5N) and Te (6N) were evaporated from Knudsen effusion cells. During growth of the TI, the substrate was maintained at ~ 240 °C. The flux ratio of Te per (Bi + Sb) was set to be >10 to prevent Te deficiency in the samples. The magnetic or nonmagnetic TI growth rate was at ~ 0.25 QL/min. Each layer of the sandwich heterostructure was grown with the different Bi/Sb ratio by adjusting their K-cell temperatures to tune the chemical potential close to its charge neutral point. Finally, to avoid possible contamination, a 10 nm thick Te layer is deposited at room temperature on top of the sandwich heterostructures prior to their removal from the MBE chamber for *ex-situ* transport and other characterization measurements.

Hall-bar device fabrications.

The magnetic TI sandwich heterostructures grown on 2 mm \times 10 mm heated-treated insulating SrTiO₃ (111) were scratched into a Hall bar geometry using a computer-controlled probe station. The effective area of the Hall bar device is ~ 1 mm \times 0.5 mm. The electrical ohmic-contacts for transport measurements were made by pressing indium spheres on the Hall bar. The bottom gate electrode was prepared through an indium foil on the back side of the SrTiO₃ substrate.

Transport measurements.

Transport measurements were conducted using both a Quantum Design Physical Property Measurement System (PPMS; 2 K, 9 T) and a Leiden Cryogenics dilution refrigerator (10 mK, 9 T) with the magnetic field applied perpendicular to the film plane. The bottom gate voltage was applied using a Keithley 6430. The excitation currents in the DC PPMS measurements (≥ 2 K) is 1 μ A. We used a PicoWatt AVS-47 AC resistance bridge to conduct the dilution refrigerator measurements (< 2 K) with a low excitation current (1 nA) to suppress heating effect. The results reported here have been reproduced on 2 samples measured in the dilution refrigerator and more than 10 samples measured in PPMS. All the transport results shown here were anti-symmetrized as a function of the magnetic field. More transport results are found in the Supplementary Information.

Theoretical calculations.

The QW Hamiltonian is $H_{QW} = \varepsilon_0(\mathbf{k}) + N(\mathbf{k})\tau_z + A(k_y\sigma_x - k_x\sigma_y)\tau_x + U\tau_x$, where Pauli matrices σ 's stand for spins and τ 's stand for two orbitals. $\varepsilon = C_0 + C_1k^2$ and $N = N_0 + N_2k^2$. Different sets of QW states differ by different C_0 and N_0 values. Dispersion in **Fig. 4c** takes values $C_0 = 0.145\text{eV}$, $C_2 = 10.0\text{eV} \cdot \text{\AA}^2$, $N_0 = -0.18\text{eV}$, $N_2 = 15.0\text{eV} \cdot \text{\AA}^2$, $A = 3.0\text{eV} \cdot \text{\AA}$, and $U = 0.02\text{eV}$. Coupling of the QW electrons to magnetization \mathbf{M} is simply $H_{Zeeman}^{QW} = -\mathbf{M} \cdot \boldsymbol{\sigma}$. On the other hand, the SSs have the Hamiltonian $H_{SS} = v_F(k_y\sigma_x - k_x\sigma_y)\tau_z + U\tau_z + m_0\sigma_x$, where σ 's again stand for spins but τ 's stand for two surfaces instead. U is the asymmetric potential applied to two surfaces. The coupling to magnetizations \mathbf{M}^t and \mathbf{M}^b on top and bottom surfaces, respectively, is $H_{Zeeman}^{SS} = \mathbf{M}^t \cdot \boldsymbol{\sigma}(1 + \tau_z)/2 + \mathbf{M}^b \cdot \boldsymbol{\sigma}(1 - \tau_z)/2$. In **Fig. 4c**, we use $m_0 = 0.005\text{eV}$, $v_F = 3.0\text{eV} \cdot \text{\AA}$, and $U = 0.02\text{eV}$.

Acknowledgments

The authors would like to thank X. D. Xu, B. H. Yan, H. Z. Lu and W. D. Wu for helpful discussions. D. X. and N. S. acknowledge support from ONR grant (N-000141512370) and Penn State 2DCC-MIP under NSF grant DMR-1539916. J. H. S. and M. H. W. C. acknowledge the support from NSF grant DMR-1707340. C. X. L. acknowledges the support from ONR grant (N00014-15-1-2675 and renewal No. N00014-18-1-2793). D. A. and J. D. Z. acknowledge the support from DOE grant (DE-SC0016424). C. Z. C. acknowledges the support from Alfred P. Sloan Research Fellowship and ARO Young Investigator Program Award (W911NF1810198). Support for transport measurements and data analysis is provided by DOE grant (DE-SC0019064).

Additional information

Supplementary information is available in the [online version of the paper](#). Reprints and permissions information is available online at www.nature.com/reprints.

Correspondence and requests for materials should be addressed to N. S., M. H. W. C. or C. Z. C.

Competing financial interests

The authors declare no competing financial interests.

Figures and figure captions

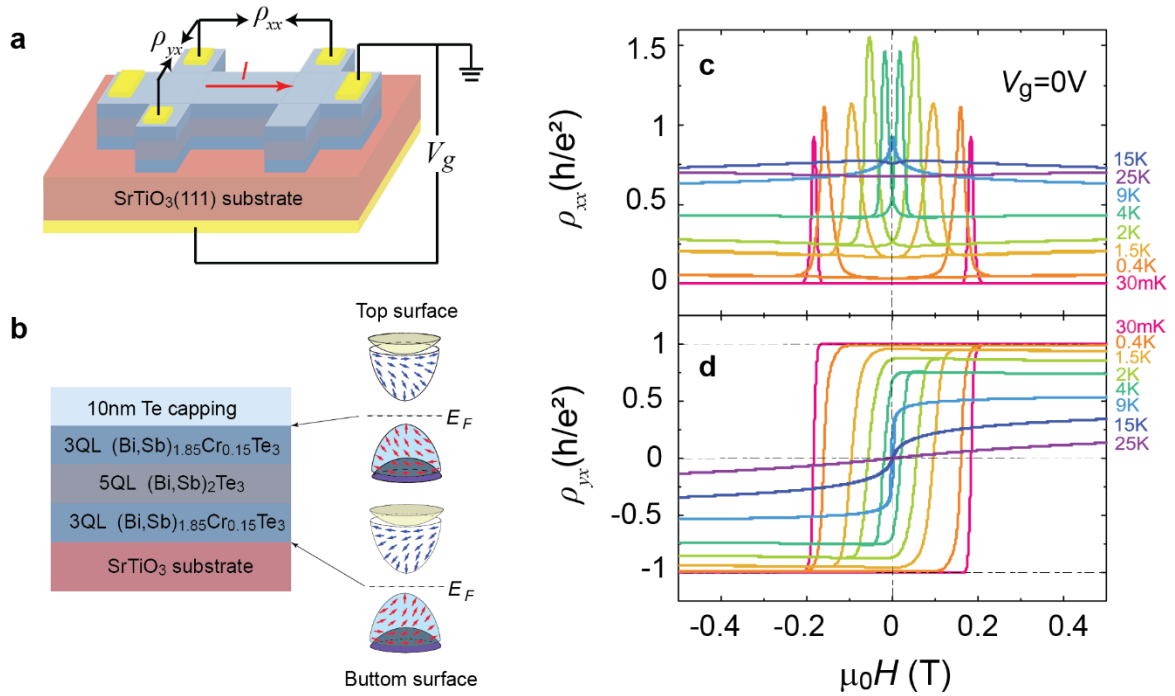


Figure 1 | QAH effect in TI sandwich heterostructures. (a) Schematic of the field-effect transistor device with a bottom gate (V_g) used in transport measurements. The electrical contacts on the Hall bar and the back-gate contact are made by pressed indium dots. The 0.5 mm SrTiO₃(111) substrate is used as the dielectric layer for the bottom gate. (b) Schematic of the magnetic TI sandwich heterostructure. The total thickness of the sample is 11QL. When $T < T_C$, an exchange gap opens at the Dirac points of the top and bottom surfaces. Blue (red) arrows in the gapped Dirac surface states represents the spin orientations. (c, d) Magnetic field $\mu_0 H$ dependence of the longitudinal resistance ρ_{xx} (c) and the Hall resistance ρ_{yx} (d) at $V_g = 0$ V. At $T = 30$ mK and $V_g = 0$ V, the quantized ρ_{yx} and the vanishing ρ_{xx} suggest this sandwich sample is in the QAH state.

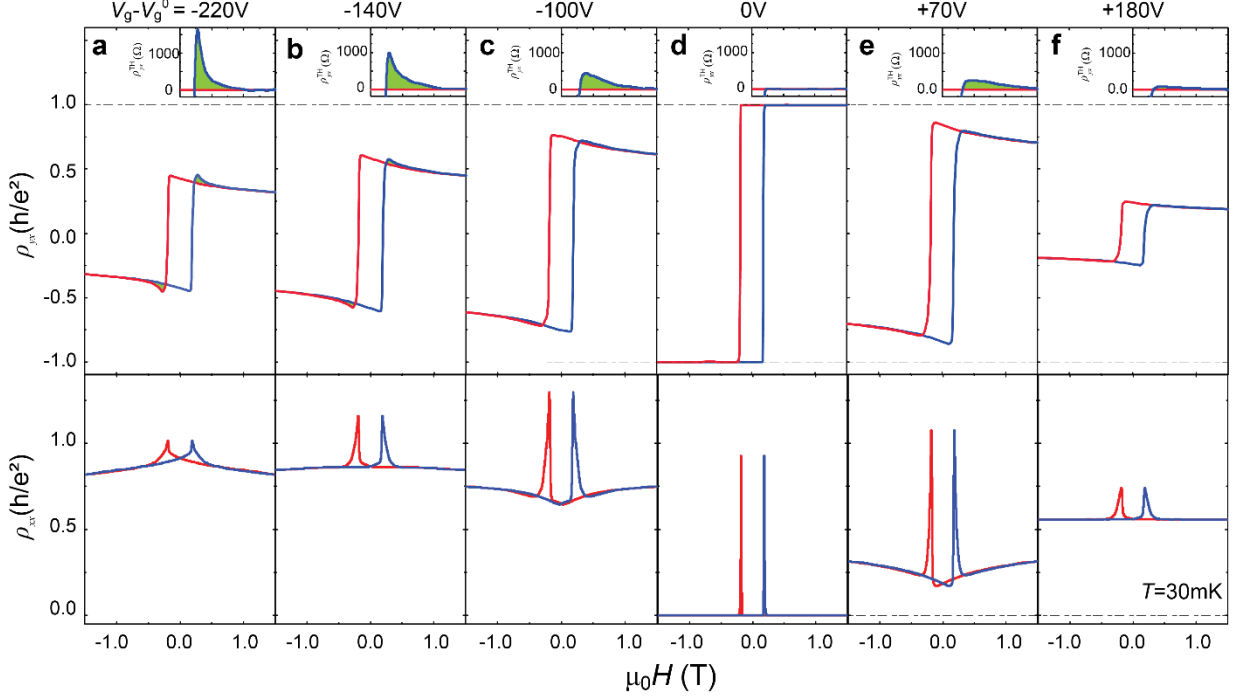


Figure 2 | Gate-induced TH effect in TI sandwich heterostructures. (a-f) Magnetic field $\mu_0 H$ dependence of the Hall resistance ρ_{yx} (top) and the longitudinal resistance ρ_{xx} (bottom) at different gates ($V_g - V_g^0$). The sample shows a perfect QAH state when $V_g = V_g^0 = +20$ V. When V_g is tuned away from V_g^0 , ρ_{yx} deviates from the quantized value (i.e., h/e^2) and shows a “hump” feature shaded in green which is known as the TH effect. Insets of (a-f) show the TH resistance ρ_{yx}^{TH} , which is subtracted using the following method: the offset resistance of ρ_{yx} when the external $\mu_0 H$ is swept upward and downward. Blue (red) curve represents the process for increasing (decreasing) $\mu_0 H$.

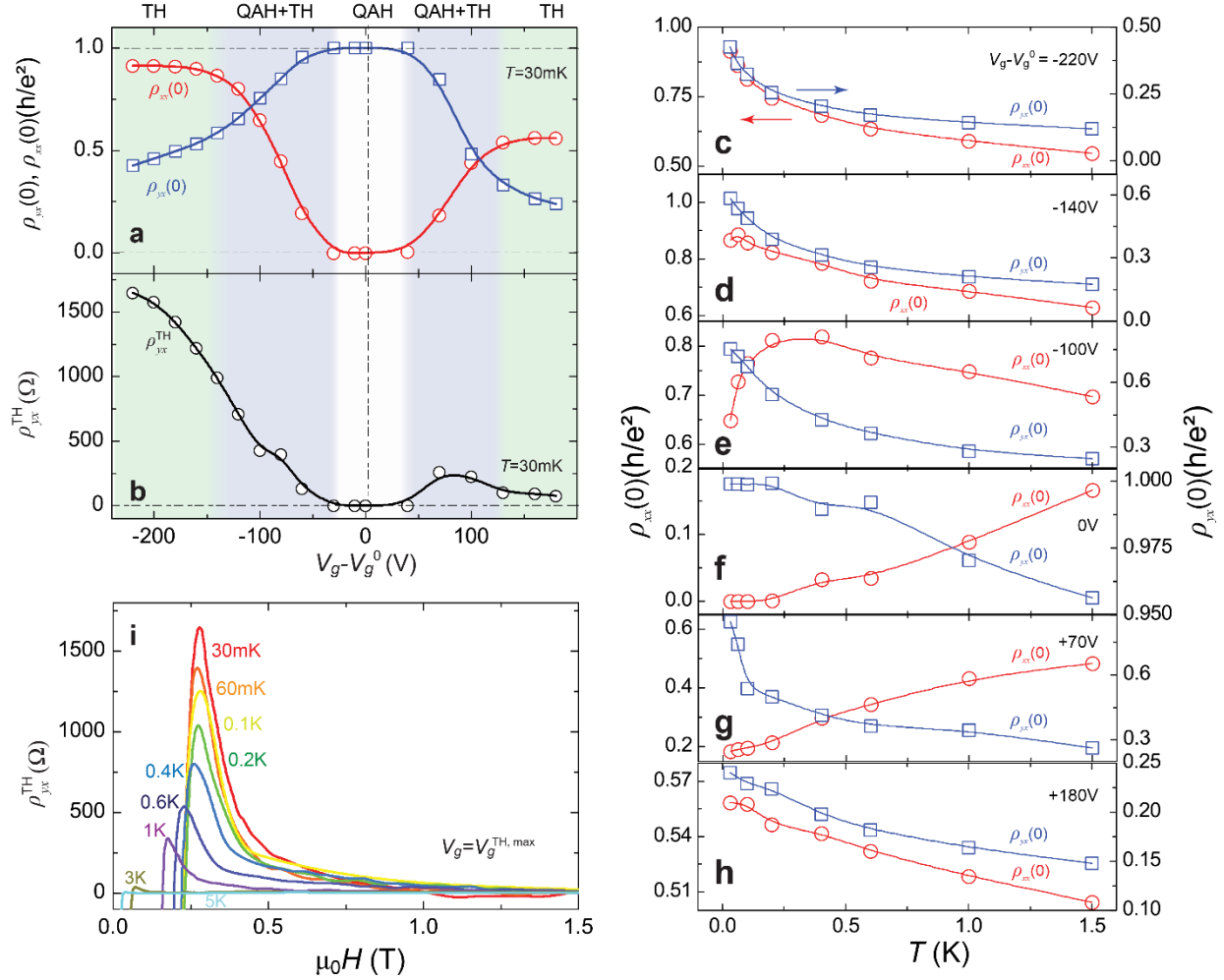


Figure 3 | Concurrence of the QAH and TH effect in TI sandwich heterostructures. (a) Gate dependence of the Hall resistance $\rho_{yx}(0)$ (empty blue squares) and the longitudinal resistance $\rho_{xx}(0)$ (empty red circles) at zero magnetic field. (b) Gate dependence of the TH resistance ρ_{yx}^{TH} . The regions of concurrence of the QAH and TH effects are shaded in light blue. (c-h) Temperature dependence of the Hall resistance $\rho_{yx}(0)$ (empty blue squares) and the longitudinal resistance $\rho_{xx}(0)$ (empty red circles) for different gates ($V_g - V_g^0$). (i) $\mu_0 H$ dependence of ρ_{yx}^{TH} for different T at $V_g = V_g^{\text{TH}, \text{max}}$. ρ_{yx}^{TH} decreases with increasing temperature. ρ_{yx}^{TH} is 1.65 K Ω at $T = 30$ mK and disappears at $T = 5$ K.

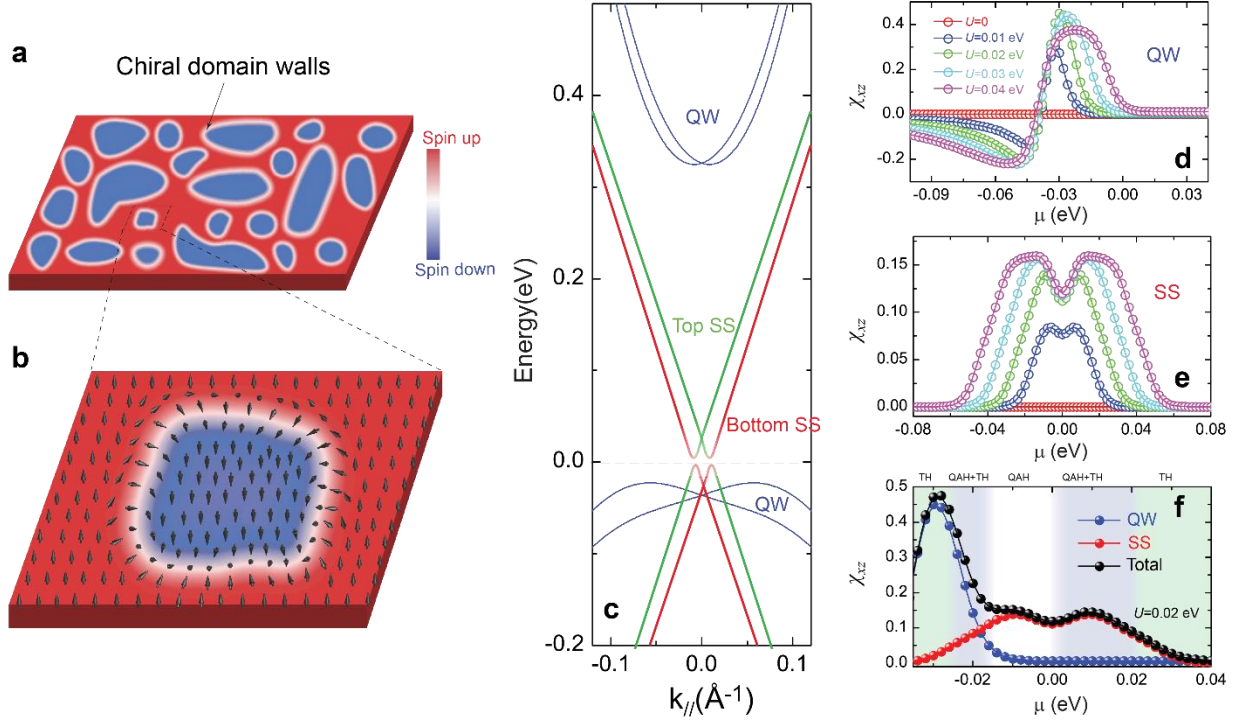


Figure 4 | Chiral domain walls and theoretical interpretations of the appearance of the TH effect. (a) The formation of the chiral domain walls during magnetization reversals. (b) A magnified view depicting the spin distribution of the chiral domain wall. (c) The energy dispersions of the surface states (SS) and bulk quantum well (QW) bands in magnetic TI. The top SS, the bottom SS, and the bulk QW are shown in green, red, and blue, respectively. (d-e) χ_{xz} as a function of chemical potential μ for the QW and SS states, respectively, under different asymmetric potentials U . (f) The QW contribution to χ_{xz} , SS contribution to χ_{xz} , and the total χ_{xz} in the magnetic TI sandwich heterostructures when $U=0.02$ eV. $q_x = 0.005 \text{ \AA}^{-1}$ and $q_y = 0$ in (d-f).

References

1. Hasan M. Z., Kane C. L. Colloquium: Topological Insulators. *Rev. Mod. Phys.* **82**, 3045-3067 (2010).
2. Qi X. L., Zhang S. C. Topological Insulators and Superconductors. *Rev. Mod. Phys.* **83**, 1057-1110 (2011).
3. Nagaosa N., Tokura Y. Topological Properties and Dynamics of Magnetic Skyrmions. *Nat. Nanotechnol.* **8**, 899-911 (2013).
4. Nagaosa N., Sinova J., Onoda S., MacDonald A. H., Ong N. P. Anomalous Hall effect. *Rev. Mod. Phys.* **82**, 1539-1592 (2010).
5. Haldane F. D. M. Model for a Quantum Hall-Effect without Landau Levels: Condensed-Matter Realization of the "Parity Anomaly". *Phys. Rev. Lett.* **61**, 2015-2018 (1988).
6. Liu C. X., Qi X. L., Dai X., Fang Z., Zhang S. C. Quantum anomalous Hall effect in $\text{Hg}_{1-y}\text{Mn}_y\text{Te}$ quantum wells. *Phys. Rev. Lett.* **101**, 146802 (2008).
7. Qi X. L., Hughes T. L., Zhang S. C. Topological Field Theory of Time-Reversal Invariant Insulators. *Phys. Rev. B* **78**, 195424 (2008).
8. Yu R., Zhang W., Zhang H. J., Zhang S. C., Dai X., Fang Z. Quantized Anomalous Hall Effect in Magnetic Topological Insulators. *Science* **329**, 61-64 (2010).
9. Chang C. Z., Zhang J. S., Feng X., Shen J., Zhang Z. C., Guo M. H., Li K., Ou Y. B., Wei P., Wang L. L., Ji Z. Q., Feng Y., Ji S. H., Chen X., Jia J. F., Dai X., Fang Z., Zhang S. C., He K., Wang Y. Y., Lu L., Ma X. C., Xue Q. K. Experimental Observation of the Quantum Anomalous Hall Effect in a Magnetic Topological Insulator. *Science* **340**, 167-170 (2013).
10. Chang C. Z., Zhao W. W., Kim D. Y., Zhang H. J., Assaf B. A., Heiman D., Zhang S. C., Liu C. X., Chan M. H. W., Moodera J. S. High-Precision Realization of Robust Quantum Anomalous Hall State in a Hard Ferromagnetic Topological Insulator. *Nat. Mater.* **14**, 473-477 (2015).
11. Checkelsky J. G., Yoshimi R., Tsukazaki A., Takahashi K. S., Kozuka Y., Falson J., Kawasaki M., Tokura Y. Trajectory of the Anomalous Hall Effect towards the Quantized State in a Ferromagnetic Topological Insulator. *Nat. Phys.* **10**, 731-736 (2014).
12. Kou X. F., Guo S. T., Fan Y. B., Pan L., Lang M. R., Jiang Y., Shao Q. M., Nie T. X., Murata K., Tang J. S., Wang Y., He L., Lee T. K., Lee W. L., Wang K. L. Scale-Invariant Quantum Anomalous Hall Effect in Magnetic Topological Insulators beyond the Two-Dimensional Limit. *Phys. Rev. Lett.* **113**, 137201 (2014).

13. Mogi M., Yoshimi R., Tsukazaki A., Yasuda K., Kozuka Y., Takahashi K. S., Kawasaki M., Tokura Y. Magnetic Modulation Doping in Topological Insulators toward Higher-Temperature Quantum Anomalous Hall Effect. *Appl. Phys. Lett.* **107**, 182401 (2015).
14. Neubauer A., Pfleiderer C., Binz B., Rosch A., Ritz R., Niklowitz P. G., Boni P. Topological Hall Effect in the A Phase of MnSi. *Phys. Rev. Lett.* **102**, 186602 (2009).
15. Lee M., Kang W., Onose Y., Tokura Y., Ong N. P. Unusual Hall Effect Anomaly in MnSi under Pressure. *Phys. Rev. Lett.* **102**, 186601 (2009).
16. Kanazawa N., Onose Y., Arima T., Okuyama D., Ohoyama K., Wakimoto S., Kakurai K., Ishiwata S., Tokura Y. Large Topological Hall Effect in a Short-Period Helimagnet MnGe. *Phys. Rev. Lett.* **106**, 156603 (2011).
17. Huang S. X., Chien C. L. Extended Skyrmion Phase in Epitaxial FeGe(111) Thin Films. *Phys. Rev. Lett.* **108**, 267201 (2012).
18. Matsuno J., Ogawa N., Yasuda K., Kagawa F., Koshibae W., Nagaosa N., Tokura Y., Kawasaki M. Interface-Driven Topological Hall Effect in SrRuO₃-SrIrO₃ Bilayer. *Sci. Adv.* **2**, e1600304 (2016).
19. Ohuchi Y., Matsuno J., Ogawa N., Kozuka Y., Uchida M., Tokura Y., Kawasaki M. Electric-Field Control of Anomalous and Topological Hall Effects in Oxide Bilayer Thin Films. *Nat. Commun.* **9**, 213 (2018).
20. Yasuda K., Wakatsuki R., Morimoto T., Yoshimi R., Tsukazaki A., Takahashi K. S., Ezawa M., Kawasaki M., Nagaosa N., Tokura Y. Geometric Hall Effects in Topological Insulator Heterostructures. *Nat. Phys.* **12**, 555-559 (2016).
21. Liu C., Zang Y. Y., Ruan W., Gong Y., He K., Ma X. C., Xue Q. K., Wang Y. Y. Dimensional Crossover-Induced Topological Hall Effect in a Magnetic Topological Insulator. *Phys. Rev. Lett.* **119**, 176809 (2017).
22. Chen Y. L., Analytis J. G., Chu J. H., Liu Z. K., Mo S. K., Qi X. L., Zhang H. J., Lu D. H., Dai X., Fang Z., Zhang S. C., Fisher I. R., Hussain Z., Shen Z. X. Experimental Realization of a Three-Dimensional Topological Insulator, Bi₂Te₃. *Science* **325**, 178-181 (2009).
23. Zhang J. S., Chang C. Z., Zhang Z. C., Wen J., Feng X., Li K., Liu M. H., He K., Wang L. L., Chen X., Xue Q. K., Ma X. C., Wang Y. Y. Band Structure Engineering in (Bi_{1-x}Sb_x)₂Te₃ Ternary Topological Insulators. *Nat. Commun.* **2**, 574 (2011).
24. Zhu J. J., Yao D. X., Zhang S. C., Chang K. Electrically Controllable Surface Magnetism on the Surface of Topological Insulators. *Phys. Rev. Lett.* **106**, 097201 (2011).
25. Ye F., Ding G. H., Zhai H., Su Z. B. Spin Helix of Magnetic Impurities in Two-Dimensional Helical Metal. *Euro. Phys. Lett.* **90**, 47001 (2010).

26. Xiao D., Jiang J., Shin J. H., Wang W. B., Wang F., Zhao Y. F., Liu C. X., Wu W. D., Chan M. H. W., Samarth N., Chang C. Z. Realization of the Axion Insulator State in Quantum Anomalous Hall Sandwich Heterostructures. *Phys. Rev. Lett.* **120**, 056801 (2018).
27. Mogi M., Kawamura M., Yoshimi R., Tsukazaki A., Kozuka Y., Shirakawa N., Takahashi K. S., Kawasaki M., Tokura Y. A Magnetic Heterostructure of Topological Insulators as a Candidate for an Axion Insulator. *Nat. Mater.* **16**, 516-521 (2017).
28. Mogi M., Kawamura M., Tsukazaki A., Yoshimi R., Takahashi K. S., Kawasaki M., Tokura Y. Tailoring Tricolor Structure of Magnetic Topological Insulator for Robust Axion Insulator. *Sci. Adv.* **3**, eaao1669 (2017).
29. Zhang Y., He K., Chang C. Z., Song C. L., Wang L. L., Chen X., Jia J. F., Fang Z., Dai X., Shan W. Y., Shen S. Q., Niu Q., Qi X. L., Zhang S. C., Ma X. C., Xue Q. K. Crossover of the Three-Dimensional Topological Insulator Bi_2Se_3 to the Two-Dimensional Limit. *Nat. Phys.* **6**, 584-588 (2010).
30. Chang C. Z., Zhang J. S., Liu M. H., Zhang Z. C., Feng X., Li K., Wang L. L., Chen X., Dai X., Fang Z., Qi X. L., Zhang S. C., Wang Y. Y., He K., Ma X. C., Xue Q. K. Thin Films of Magnetically Doped Topological Insulator with Carrier-Independent Long-Range Ferromagnetic Order. *Adv. Mater.* **25**, 1065-1070 (2013).
31. Zhang Z. C., Feng X., Guo M. H., Li K., Zhang J. S., Ou Y. B., Feng Y., Wang L. L., Chen X., He K., Ma X. C., Xue Q. K., Wang Y. Y. Electrically Tuned Magnetic Order and Magnetoresistance in a Topological Insulator. *Nat. Commun.* **5**, 4915 (2014).
32. Chang C. Z., Zhao W. W., Kim D. Y., Wei P., Jain J. K., Liu C. X., Chan M. H. W., Moodera J. S. Zero-Field Dissipationless Chiral Edge Transport and the Nature of Dissipation in the Quantum Anomalous Hall State. *Phys. Rev. Lett.* **115**, 057206 (2015).
33. Wang W. B., Ou Y. B., Liu C., Wang Y. Y., He K., Xue Q. K., Wu W. D. Direct Evidence of Ferromagnetism in a Quantum Anomalous Hall System. *Nat. Phys.* **14**, 791-795 (2018).
34. Jiang W. J., Chen G., Liu K., Zang J. D., te Velthuis S. G. E., Hoffmann A. Skyrmions in Magnetic Multilayers. *Phys. Rep.* **704**, 1-49 (2017).
35. Hou W. T., Yu J. X., Daly M., Zang J. D. Thermally Driven Topology in Chiral Magnets. *Phys. Rev. B* **96** (2017).
36. Bottcher M., Heinze S., Egorov S., Sinova J., Dupe B. B-T Phase Diagram of Pd/Fe/Ir(111) Computed with Parallel Tempering Monte Carlo. *New J. Phys.* **20**, 103014 (2018).
37. Wang W., Daniels M. W., Liao Z., Zhao Y., Wang J., Koster G., Rijnders G., Chang C.-Z., Xiao D., Wu W. Universal Spin Chirality Fluctuation in Two-Dimensional Ising Ferromagnets. *arXiv:1812.07005* (2018).

38. Liu C. X., Zhang H., Yan B. H., Qi X. L., Frauenheim T., Dai X., Fang Z., Zhang S. C. Oscillatory Crossover from Two-Dimensional to Three-Dimensional Topological Insulators. *Phys. Rev. B* **81**, 041307 (2010).
39. Li W., Claassen M., Chang C. Z., Moritz B., Jia T., Zhang C., Rebec S., Lee J. J., Hashimoto M., Lu D. H., Moore R. G., Moodera J. S., Devereaux T. P., Shen Z. X. Origin of the Low Critical Observing Temperature of the Quantum Anomalous Hall Effect in V-Doped (Bi, Sb)₂Te₃ Film. *Sci. Rep.* **6**, 32732 (2016).
40. Moriya T. Anisotropic Superexchange Interaction and Weak Ferromagnetism. *Phys. Rev.* **120**, 91-98 (1960).
41. Groenendijk D. J., Autieri C., Thiel T. C. v., Brzezicki W., Gauquelin N., Barone P., van den Bos K. H. W., van Aert S., Verbeeck J., Filippetti A., Picozzi S., Cuoco M., Caviglia A. D. Berry Phase Engineering at Oxide Interfaces. *arXiv:1810.05619* (2018).